

Updating the ⁵⁶Ni Problem in Core-collapse Supernova Explosion

RYO SAWADA ¹ AND YUDAI SUWA ^{1,2}

¹*Department of Earth Science and Astronomy, Graduate School of Arts and Sciences, The University of Tokyo, Tokyo 153-8902, Japan*

²*Center for Gravitational Physics and Quantum Information, Yukawa Institute for Theoretical Physics, Kyoto University, Kyoto 606-8502, Japan*

Submitted to ApJ

ABSTRACT

Details of the core-collapse supernova (CCSN) explosion mechanism still need to be fully understood. There is an increasing number of successful examples of reproducing explosions in multidimensional hydrodynamic simulations, but subsequent studies pointed out that the growth rates of the explosion energy \dot{E}_{expl} of these simulations are insufficient to produce enough ⁵⁶Ni to match observations. This issue is known as the ‘⁵⁶Ni problem’ in CCSNe. Recently, however, some studies have suggested that this ⁵⁶Ni problem is derived from the simplicity of the explosion model. In response, we investigate the effect of the explosion energy growth rate \dot{E}_{expl} on the behavior of nucleosynthesis in CCSNe in a more realistic model. We employ the 1D Lagrangian hydrodynamic code, in which we take neutrino heating and cooling terms into account with the light-bulb approximation. We reiterate that, consistent with previous rebuttal studies, there is the ⁵⁶Ni problem: Although ⁵⁶Ni is synthesized to almost the same mass coordinate independent of \dot{E}_{expl} , some of the innermost material in the low- \dot{E}_{expl} model failed to escape, leading to a shift in the innermost mass coordinate of the ejecta to the outer positions. Comparing our results with observations, we find that while modern slow explosions can, in principle, reproduce observations of standard Type II SNe, this is not possible with stripped-envelope SNe. Our finding places a strong constraint on the explosion mechanism. There are significant differences in the progenitor structures and the explosion mechanism between Type II and stripped-envelope SNe.

Keywords: (stars:) supernovae: general—hydrodynamics

1. INTRODUCTION

Radioisotope ⁵⁶Ni is an important product in supernova nucleosynthesis, which drives supernova (SN) brightness. ⁵⁶Ni decays into ⁵⁶Co, and then into ⁵⁶Fe. This nuclear decay chain powers the light curve of SNe, and thus, ⁵⁶Ni masses of SNe have been estimated with reasonable accuracy from the light curve (see, e.g., Ar-

nett 1982; Hamuy 2003).¹ On the other hand, the amount of synthesized ⁵⁶Ni is sensitive to the temperature T , the density ρ , and the number of electrons per nucleon (electron fraction) Y_e , i.e., explosion property and pre-SNe core structure (e.g., Woosley & Weaver 1995; Thielemann et al. 1996; Woosley et al. 2002). These two factors, that is, the amount of ⁵⁶Ni synthesis can be accurately estimated from observations and strongly reflect the explosion’s innermost nature, suggest the following. ⁵⁶Ni is the best probe to constrain an

Corresponding author: Ryo Sawada
ryo@g.ecc.u-tokyo.ac.jp

¹ For Type-II SNe, the tail luminosity provides ⁵⁶Ni mass, assuming the complete trapping of γ -rays produced from the nuclear decay. For Type-I SNe, on the contrary, the peak luminosity has often been used, assuming that it should be equal to the instantaneous energy deposition rate by the nuclear decay, so-called Arnett rule (Arnett 1982). Core-collapse SNe in the latter category is called stripped-envelope SNe (SE-SNe; Smartt 2009).

aspect of the SN explosion mechanism accurately (e.g., Maeda & Tominaga 2009; Suwa & Tominaga 2015).

Details of the explosion mechanism of core-collapse supernovae (CCSNe) are not yet fully understood. The most promising scenario is the delayed neutrino-driven explosion (Bethe & Wilson 1985). While this scenario had once not been reproduced by numerical simulations, the situation has brought substantial progress over a few decades. Now, there is an increasing number of successful examples of reproducing explosions in multidimensional hydrodynamic simulations, with a detailed neutrino transport (see, e.g., Lentz et al. 2015; Takiwaki et al. 2016; Müller et al. 2017; O’Connor & Couch 2018; Glas et al. 2019; Bollig et al. 2021; Burrows & Vartanyan 2021; Bruen et al. 2022, and references therein). Although the details now depend on the numerical methods and physical approximations employed in each simulation, there seems to be a general understanding that the explosion succeeds by the growth of the hydrodynamic instability over a sufficient time. Indeed, most, if not all, of those state-of-the-art simulations, have shown a slow increase of explosion energy, and the growing rate of the explosion energy is typically $\dot{E}_{\text{expl}} = \mathcal{O}(0.1)$ Bethe s^{-1} (1 Bethe $\equiv 1 \times 10^{51}$ erg), especially for 3D simulations.

However, recent several studies have shown that to reproduce the typical observed mass of ^{56}Ni by the explosive nucleosynthesis in the ejecta, the growth rate of the explosion energy of $\dot{E}_{\text{expl}} = \mathcal{O}(1)$ Bethe s^{-1} is required in several methods (Sawada & Maeda 2019; Suwa et al. 2019; Saito et al. 2022). Sawada & Maeda (2019) found the inverse-correlation between ^{56}Ni yield and explosion energy growth rate \dot{E}_{expl} by 1D simulations with the simple thermal-bomb modeling and post-processing detailed-nucleosynthesis, and Suwa et al. (2019) also came to the same conclusion by conducting hydrodynamic simulations with an approximate neutrino heating model that self-consistently follows core-collapse and shock-revival. Saito et al. (2022) also confirmed this trend, using the same method as Sawada & Maeda (2019), but modeled for individual objects to reduce observational uncertainties. If these results are correct, the current multi-D simulations, which give explosion energy growth rates of $\dot{E}_{\text{expl}} = \mathcal{O}(0.1)$ Bethe s^{-1} , would be observationally unfavorable. We refer to this issue as the nickel mass problem (^{56}Ni problem,’ hereafter) in this paper. However, this ^{56}Ni problem is still under some debate.

In particular, Imasheva et al. (2023) just recently pointed out the most obvious question to the ^{56}Ni problem. Imasheva et al. (2023) used the same method as Sawada & Maeda (2019), with simple thermal injection

modeling and post-processing detailed nucleosynthesis, but scrutinized the treatment of initial conditions. In the recent slow explosion scenario, the pre-SN star experiences sufficient gravitational contraction just before the successful explosion. They found that the correlation between ^{56}Ni yield and explosion energy growth rate \dot{E}_{expl} is the result of ignoring this initial collapse. They argued that this correlation disappears when the initial collapse is included and also that further initial collapse inversely results in more ^{56}Ni being synthesized in slower explosions.

Their arguments also apply to Sawada & Maeda (2019) and Saito et al. (2022), but not to Suwa et al. (2019). Suwa et al. (2019) solved self-consistently the core collapse and shock revival with the light-bulb scheme and found this correlation even though they took into account the initial collapse phase. This result is inconsistent with the conclusion of Imasheva et al. (2023). Note that Suwa et al. (2019) performed no detailed nucleosynthesis calculations. Instead, they estimated the ^{56}Ni amount simply by the temperature of hydrodynamic simulations. Therefore, we perform hydrodynamic and detailed nucleosynthesis calculations in this study. This study aims to clarify the detailed picture of how ^{56}Ni synthesis occurs in the current CCSN explosion scenario. By clarifying this picture, we also expect to explain the origin of the differences between the two studies and, by extension, the cause of the ^{56}Ni problem itself.

In this paper, therefore, we simulate one-dimensional hydrodynamics in the light-bulb scheme as in Suwa et al. (2019), then perform detailed nucleosynthesis in a post-process manner. The goal of this study is to present a detailed picture of ^{56}Ni nucleosynthesis in CCSNe with self-consistent explosion modeling. Furthermore, we aim to sort out the controversial ^{56}Ni problem. In Section 2, we describe our simulation methods, the progenitor models, and post-processing analysis. Our results are summarized in Section 3. In Section 4, we revisit the ^{56}Ni problem through a detailed comparison of our results and observations, and discuss the uncertainties involved. We conclude in Section 5.

2. SIMULATION METHODS

Following the computational setup performed in Suwa et al. (2019), we employ a 1D Lagrangian Newtonian hydrodynamic code based on `blcode`.² Basic equations under a spherically symmetric configuration, as we per-

² This code is a prototype code of SNEC (Morozova et al. 2015), and available from <https://stellarcollapse.org>

form in this paper, are given as follows:

$$\frac{\partial r}{\partial M_r} = \frac{1}{4\pi r^2 \rho}, \quad (1)$$

$$\frac{Dv}{Dt} = -\frac{GM_r}{r^2} - 4\pi r^2 \frac{\partial P}{\partial M_r}, \quad (2)$$

$$\frac{D\epsilon}{Dt} = -P \frac{D}{Dt} \left(\frac{1}{\rho} \right) + \mathcal{H} - \mathcal{C}, \quad (3)$$

where r is the radius, M_r is the mass coordinate, t is time, ρ is the density, v is the radial velocity, P is pressure, ϵ is the specific internal energy, and $D/Dt \equiv \partial/\partial t + v_r \partial/\partial r$ is the Lagrangian time derivative. The artificial viscosity of [Von Neumann & Richtmyer \(1950\)](#) is employed to capture a shock. The system of equations (1)-(3) is closed with the Helmholtz equation of state ([Timmes & Swesty 2000](#)), which describes the stellar plasma as a mixture of arbitrarily degenerate and relativistic electrons and positrons, black-body radiation, and ideal Boltzmann gases of a defined set of fully ionized nuclei, taking into account corrections for the Coulomb effects.

In this work, neutrino heating and cooling are added by a light-bulb scheme. In the light-bulb scheme, neutrino cooling is given as a function of temperature, and neutrino heating is a function of the radius with parameterized neutrino luminosity. The heating term \mathcal{H} and the cooling term \mathcal{C} , terms in Equation (3) are assumed to be

$$\mathcal{H} = 1.544 \times 10^{20} \text{ erg g}^{-1} \text{ s}^{-1} \times \left(\frac{L_{\nu_e}}{10^{52} \text{ MeV}} \right) \left(\frac{r_{\nu_e}}{100 \text{ km}} \right)^{-2} \left(\frac{T_{\nu_e}}{4.0 \text{ MeV}} \right)^2, \quad (4)$$

$$\mathcal{C} = 1.399 \times 10^{20} \text{ erg g}^{-1} \text{ s}^{-1} \times \left(\frac{T}{2.0 \text{ MeV}} \right)^6. \quad (5)$$

Here, we fix the neutrino temperature as $T_{\nu_e} = 4 \text{ MeV}$. We take into account these terms only in the post-shock regime. We modified the inner boundary conditions so that the innermost mass shell does not shrink within 50 km from the center to mimic the existence of a proto-neutron star (PNS). Also, the light-bulb scheme in this study tends to overestimate the neutrino-driven wind from the PNS surface at the post-explosion phase because it keeps giving a constant neutrino luminosity. Therefore, in this study, we consider the mass coordinate that experienced $r < 200 \text{ km}$ as the neutrino-driven wind and separate it from the ejecta.

The numerical computational domain contains $1.5M_{\odot}$ and uses a 1500 grid with a mass resolution of $10^{-3}M_{\odot}$. We set the inner boundary at $M_{s/k_b=4} - 0.5M_{\odot}$ for each

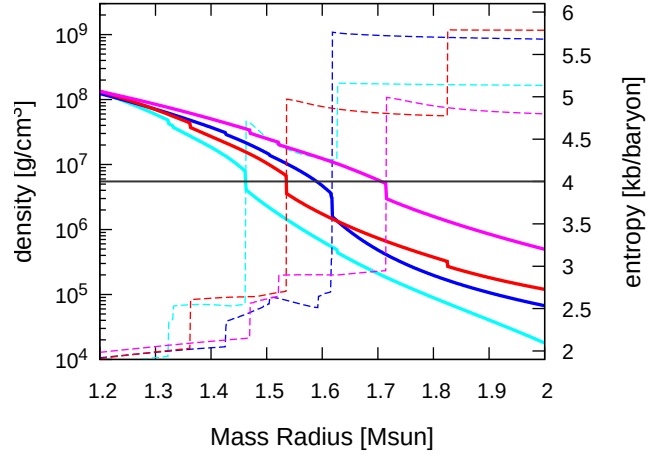
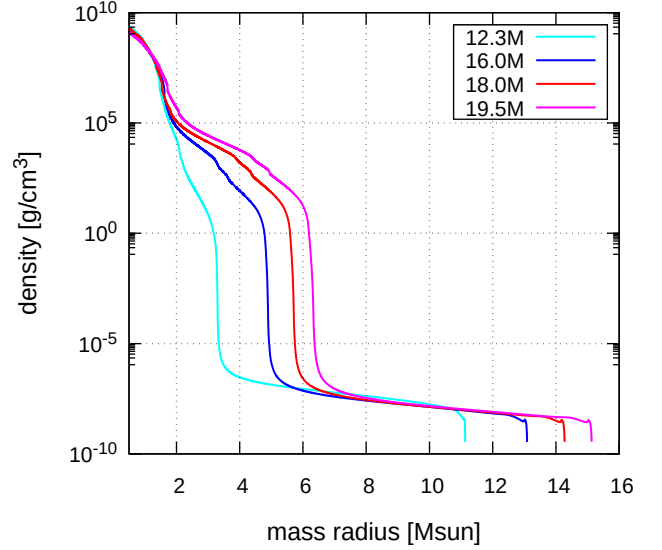


Figure 1. Density structure as a function of the enclosed mass for the considered progenitors with $M_{\text{ZAMS}} = 12.3M_{\odot}$ (cyan line), $16.0M_{\odot}$ (blue line), $19.7M_{\odot}$ (red line), and $21.0M_{\odot}$ (magenta line), and its details with the entropy per nucleon.

pre-explosion star. Each mass coordinate captures the time evolution of the hydrodynamic quantities, so that nucleosynthesis calculations are performed as a post-processing analysis with this trajectory. We calculate a reaction network of 640 nuclear species with the `torch` code ([Timmes 1999](#)).

The initial conditions adopted in this study are a subset of non-rotating stars with solar metallicity, which evolved from the main sequence to the onset of iron-core collapse, as published by [Sukhbold et al. \(2018\)](#). The physics of this set of progenitors was discussed in detail in this literature. Figure 1 shows the density structures

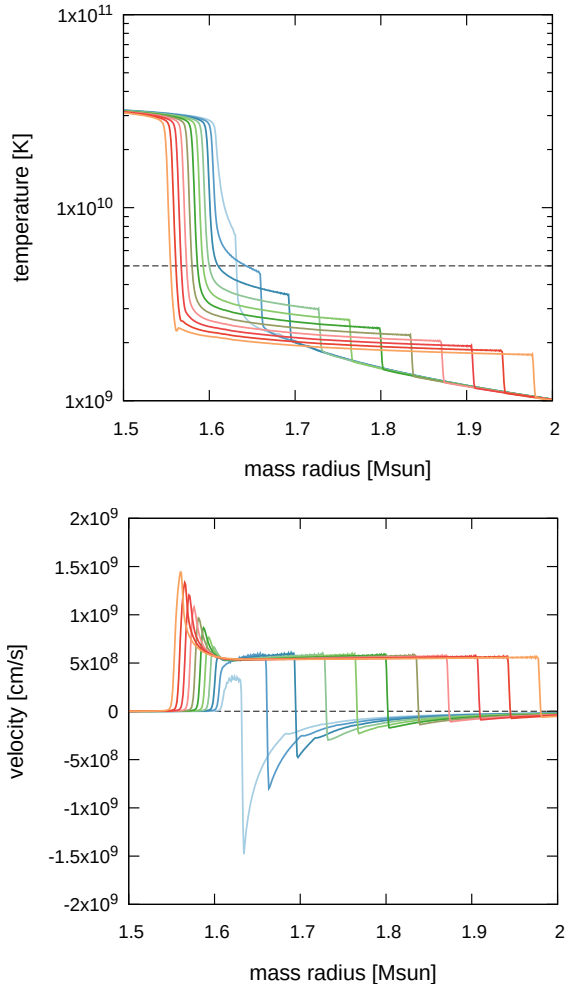


Figure 2. Time evolution of the velocity (top) and the temperature (bottom) as a function of the mass coordinate for model $16.0M_{\odot}$. In both panels, each snapshot time corresponds to approximately every 0.1 seconds from 0.5 seconds to 1.5 seconds from the start of the simulation. The gray line corresponds to $T = 5 \times 10^9$ K.

of the progenitor as a function of the enclosed mass, and its details with the entropy per nucleon.

3. RESULT

3.1. Overview of the explosion dynamics

Figure 2 shows the time evolution of radial velocity and temperature as a function of the mass coordinate for the model $16.0M_{\odot}$. We first use an example of a model with $M_{\text{ZAMS}} = 16.0M_{\odot}$ throughout this section. From the velocity figure, it can be seen that the shock begins to propagate outward from the point where the silicon/oxygen (Si-O) layer ($\approx 1.62M_{\odot}$) accretes onto the shock wave, due to the rapid decrease in ram pressure (Marek & Janka 2009; Suwa et al. 2016). From the temperature figure, we can confirm that the post-shock

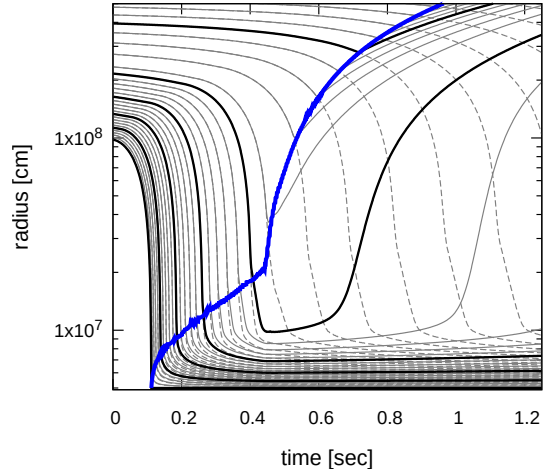


Figure 3. Radius evolution of Lagrangian mass shells with time for the explosion ($L_{\nu} = 3 \times 10^{52} \text{ erg s}^{-1}$) and non-exploding model ($L_{\nu} = 0 \text{ erg s}^{-1}$) of $16.0M_{\odot}$. The thick black solid lines are the mass shells, spaced in steps of $0.1 M_{\odot}$, and the thin gray solid/dashed lines are spaced in steps of $0.02 M_{\odot}$. The difference between the dotted and solid lines corresponds to the explosion and non-exploding models, respectively. The blue line marks the shock radius of the explosion model.

temperature of the ejecta is spatially almost constant so we define the shock temperature as the temperature of the material just behind the shock wave.

Figure 3 shows that the mass shell until the arrival of the shock in the explosion model is consistent with its behavior in the non-exploding model. In other words, we can confirm that the behavior of the mass shell up to the arrival of the shock is independent of the explosion detail. Thus, by overlaying the shock evolution on the trajectory of the mass shell in the non-exploding model, we can compare several models at once to see where the shock impacts each of the mass shells.

In the following subsections, we present the results focusing on the effect of the explosion energy growth rate \dot{E}_{expl} on ^{56}Ni nucleosynthesis. The results are summarized in Table 1. These yields consist only of unbound ^{56}Ni by gravity as determined by a 10-second simulation. We first use an example of a model with $M_{\text{ZAMS}} = 16.0M_{\odot}$ throughout Sections 3.2 and 3.3.

3.2. Hydrodynamics and ^{56}Ni Synthesis Region

Figure 4 shows the time evolution of the shock for the models $L_{\nu} = 3, 5, \text{ and } 7 \times 10^{52} \text{ erg s}^{-1}$ and the trajectory of the mass shell in the unexploded model. In each model, the time evolutions of the shock are shown by colored lines for the range where the shock satisfies $T_9 > 5$ ($T_9 \equiv T/10^9 \text{ K}$), and by black dashed lines for the range where $T_9 < 5$. We refer to the mass coordinate that can

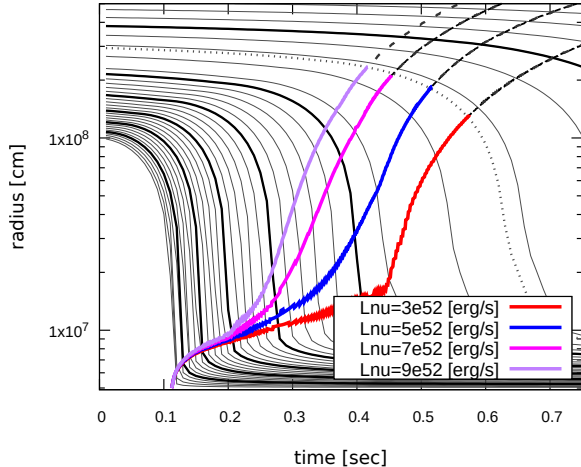


Figure 4. The time evolution of the shock radius in models $L_\nu = 3, 5,$ and 7×10^{52} erg s^{-1} with the mass shell trajectory in the unexploded model, on the time-radius plane.

spread at the shock temperature of $T_9 \approx 5$ as $M_{T_9=5}$. We find that in all models $M_{T_9=5}$ is near the mass coordinate with the enclosed mass $\approx 1.65M_\odot$, which is indicated by the dotted line in Figure 4. More detailed values are given in Table 1, and this trend is almost universal, independent of the progenitor models. In all models, we find that $M_{T_9=5}$ is near the mass coordinate with an enclosed mass of approximately $1.65M_\odot$, as indicated by the dotted line in Figure 4. More detailed values are given in Table 1, and this trend is nearly universal and independent of the progenitor models.

Qualitatively, this can be understood by using a zero-order approximation to estimate the shock radius at which the shock temperature is $T_9 = 5$. When applying a simple fireball model in which the region behind the shock wave is uniform and dominated by radiation pressure (e.g., Woosley et al. 2002), we can estimate the following relation between the temperature T , the shock radius r_{sh} and the explosion energy E_{expl} as follows:

$$E_{\text{expl}} = \frac{4\pi}{3} r_{\text{sh}}^3(t) a T^4, \quad (6)$$

where a is the radiation constant. Then with $E_{\text{expl}}(t) \equiv 10^{51}$ ergs, the radius with $T_9 = 5$ ($r_{T_9=5}$) can be estimated as follows:

$$r_{T_9=5} \approx 3.6 \times 10^8 (E_{\text{expl}}/10^{51})^{1/3} \text{ cm}. \quad (7)$$

This estimated radius is classically well-known (e.g., Woosley et al. 2002; Nomoto et al. 2013). If we consider the time evolution of $E_{\text{expl}}(t) = \dot{E}_{\text{expl}} \cdot t$, this classical radius is satisfied with an adequate large \dot{E}_{expl} . However, at the shock velocity $V_{\text{sh}} = 10^9$ cm s^{-1} , it takes less than

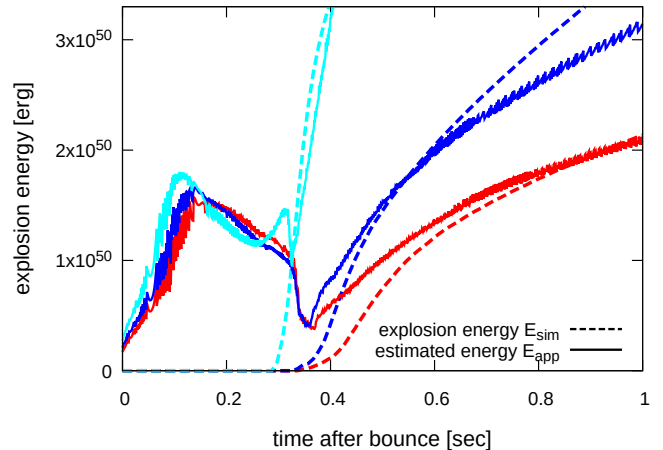


Figure 5. Comparison of the explosion energy in the simulation E_{sim} (dashed line) with the estimated energy in the fireball approximation E_{app} (solid line), which comes from Eq (8) in models $L_\nu = 2, 3,$ and 5×10^{52} erg s^{-1} . The horizontal axis is the post-bounce time.

1 second to reach this radius. In other words, if the case of $\dot{E}_{\text{expl}} \lesssim 1$ Bethe s^{-1} , it takes a few seconds to reach 1 Bethe, and obviously, the radius of $T_9 = 5$ will be small. In fact, from Figure 4, we can confirm that even in this simulation, the radius of $T_9 = 5$ is reduced in the case of low- \dot{E}_{expl} . But at the same time, the time evolution of the shock radius is also slower down for lower- \dot{E}_{expl} models, and the mass shell falls more inward due to collapse. Eventually, the ‘mass coordinate’ of $M_{T_9=5}$ seems to be approximately the same regardless of the \dot{E}_{expl} .

This result suggests a very interesting trend. ^{56}Ni is synthesized mainly by complete Si burning at $T \gtrsim 5 \times 10^9$ K (see in detail in Appendix A and Woosley et al. 1973). Thus, this hydrodynamical result suggests that the outermost mass coordinates, where ^{56}Ni is primarily synthesized, are insensitive to the explosion energy growth rate \dot{E}_{expl} . To confirm this trend in more detail, we next discuss the results of nucleosynthesis calculations.

Although this is not relevant to the main focus of this paper, we show in Figure 5 for reference the comparison of the explosion energy in the simulation E_{sim} with the estimated energy in the fireball approximation E_{app} . The explosion energy E_{sim} in the hydrodynamical simulation is defined as the integral of the sum of specific internal, kinetic, and gravitational energies over all zones, in which it is positive. The estimated energy in the fireball approximation E_{app} is given by the following equation using only the shock radius r_{sh} and shock

temperature T :

$$E_{\text{app}} = \frac{4\pi}{3} r_{\text{sh}}^3(t) aT^4 f(T_9), \quad (8)$$

where $f(T_9) = 1 + (7/4) \cdot T_9^2 / (T_9^2 + 5.3)$ is a correction term to account for both radiation pressure and non-degenerate electron-positron pairs (e.g., [Freiburghaus et al. 1999](#)). As Figure 5 shows, this simple estimation is able to reproduce the explosion energy of the simulation with good enough accuracy. This supports the validity of the above discussion, and also suggests that thermal energy is dominant in the early phases of the explosion.

3.3. Nucleosynthesis: Distribution of ^{56}Ni synthesis

Figure 6 shows the abundance distribution as a function of the mass coordinate, for $L_\nu = 3, 5,$ and 7×10^{52} erg s^{-1} with $16.0M_\odot$. As shown in Figure 6, focusing specifically on ^{56}Ni , we can confirm that the outermost mass radius, where ^{56}Ni is primarily synthesized, is in a similar position independent of the explosion energy growth rate \dot{E}_{expl} . In Table 1, we show the outermost mass radius where ^{56}Ni is largely synthesized (here, we define it as $X(^{56}\text{Ni}) > 0.5$). However, at the same time, the innermost mass radius, which is gravitationally unbounded, depends strongly on the explosion energy growth rate \dot{E}_{expl} .

4. DISCUSSION: UPDATE ‘NI PROBLEM’

Figure 7 shows the synthesized amount of ^{56}Ni as a function of the explosion energy growth rate \dot{E}_{expl} . It can be clearly seen that there is a decreasing trend of the synthesized amount of ^{56}Ni toward decreasing \dot{E}_{expl} . The reason for this trend is explained in section 3.3, but this figure tells us that the same trend is generally observed regardless of the mass and structure of the progenitor.

For comparison with observations, in Figure 7, we adopted two typical values based on a recent systematic survey for more than 300 events of CCSNe; $0.07M_\odot$ ³ as the median estimated from stripe-envelope supernovae (SE-SNe) and $0.03M_\odot$ from Type-II SNe ([Rodríguez et al. 2021, 2022](#)). Note that the figure plots the synthesized amount of ^{56}Ni ; not all ^{56}Ni can be ejected. In other words, the figure shows the maximum amount of

^{56}Ni that can be ejected by each CCSN model, and if the calculated mass of ^{56}Ni is larger than the observed value, then the model can reproduce the observed value. First, compared to the median value of Type II supernovae $0.03M_\odot$, even a modern slow explosion ($\dot{E}_{\text{expl}} \lesssim 1$ Bethe s^{-1}) provides enough amount of ^{56}Ni to reproduce the observations. On the other hand, compared to the SE-SNe median of $0.07M_\odot$, a very rapid explosion of $\dot{E}_{\text{expl}} \gtrsim 2$ Bethe s^{-1} is required to reproduce this value. This translates to a time scale of $t \lesssim 0.5$ seconds to the typical explosion energy ~ 1.0 Bethe, and this timescale is very difficult to reproduce with current multi-D self-consistent calculations.

Here we discuss a few caveats in this problem as follows.

1. [Observation of Type-II SNe]

The typical ^{56}Ni mass of canonical-CCSNe has been extensively discussed by large-scale observations in recent years. In particular, Type II SNe, when volume-limited, account for nearly $\sim 60\%$ of the observed CCSNe (e.g., [Li et al. 2011](#); [Jones et al. 2021](#)). Recently, Type II SNe have been found to have lower median nickel masses than SE-SNe (e.g., [Anderson 2019](#)), confirming that this is not due to observational bias ([Ouchi et al. 2021](#)). Furthermore, the observed kinetic energy is also found to have a lower median value than the classical typical value (~ 0.6 Bethe; [Martinez et al. 2022](#)). These facts also support the possibility that the ‘slow’ explosion results in the current state-of-the-art simulations are relatively consistent with standard Type II SNe. However, nickel synthesis and explosion energy ($M_{\text{Ni}} \approx 0.03M_\odot$ and $E_{\text{expl}} \sim 0.6$ Bethe) still remain important benchmarks for multidimensional self-consistent simulations, and it should be checked whether they are truly achieved. And, another important point is that this is only a statement of the median. According to [Ouchi et al. \(2021\)](#), the fitting function for the cumulative histogram for observed ^{56}Ni masses of each CCSNe is $f(x) = \tanh(14.60 \times x)$ ⁴ as a variable of observed ^{56}Ni masses. This roughly implies that more than 20% of the Type II supernovae synthesize ^{56}Ni above $0.075M_\odot$. While $0.03M_\odot$ is a somewhat explainable value, this value is challenging to reproduce in multi-D self-consistent simulations. So, we need to explain and

³ The $\sim 0.07M_\odot$ is often adopted as a typical value obtained for well-studied nearby SNe is on average (e.g., SN 1987A, SN 1994I, SN 2002ap; [Arnett et al. 1989](#); [Iwamoto et al. 1994](#); [Mazzali et al. 2002](#)) and we adopt this value in previous studies. However, in this study, we clearly mention here that we do not use $0.07M_\odot$ in the context of the typical for nearby SNe because we consider observational constraints from recently updated large-scale observational data.

⁴ This function is obtained by fitting non-linear least squares of observed reports of Type II SNe with a sample size of 115 events ([Ouchi et al. 2021](#)).

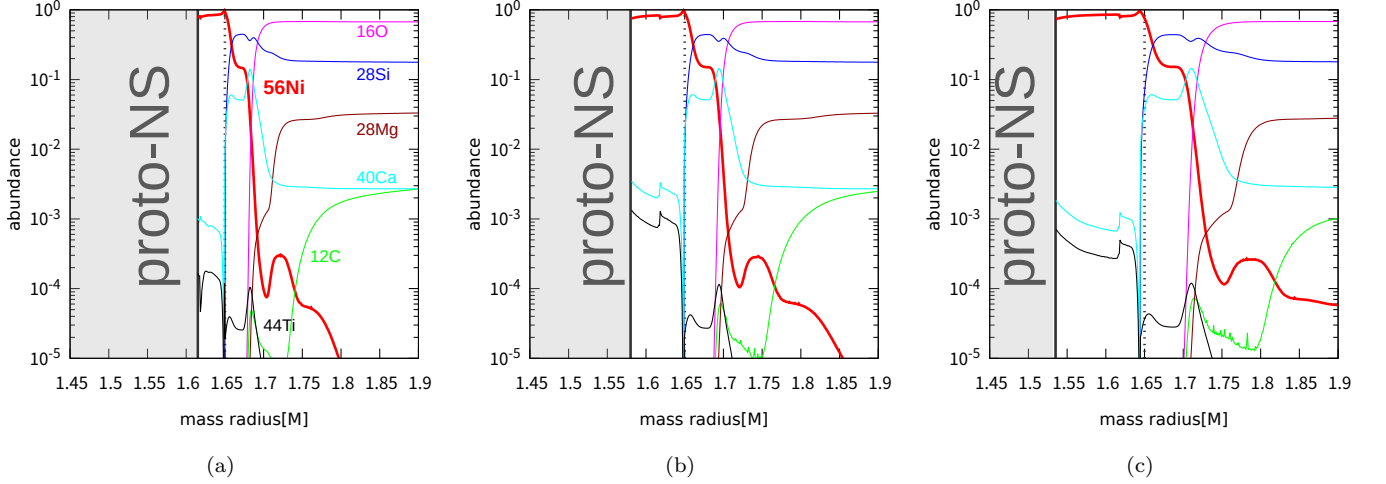


Figure 6. Abundance distribution as a function of the enclosed mass Mr , for (a) $L_\nu = 3 \times 10^{52} \text{ erg s}^{-1}$, (b) $L_\nu = 5 \times 10^{52} \text{ erg s}^{-1}$, and (c) $L_\nu = 7 \times 10^{52} \text{ erg s}^{-1}$. All the models here are with $16.0M_\odot$ of Sukhbold et al. (2018). In all panels, the vertical dotted grey line indicates the location of the mass shell with an enclosed mass $1.65M_\odot$.

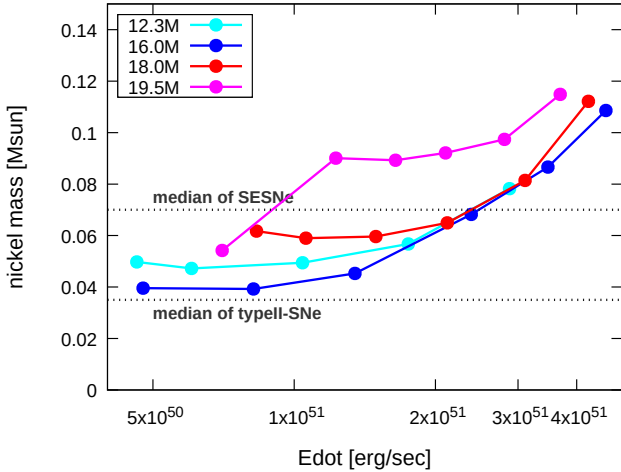


Figure 7. The amount of ^{56}Ni as a function of the growth rate of the explosion energy, \dot{E}_{expl} . The gray line indicates a typical value of ^{56}Ni , $0.07M_\odot$.

reproduce the high ^{56}Ni objects that will exist to some extent.

2. [Multidimensional effect]

How the amount of synthesized ^{56}Ni changes in a multi-D explosion model is one of the issues to be discussed. Since this model is a 1D model and explodes only with thermal energy as shown in Figure 5, the temperature should be higher than the multi-D model, especially considering the geometric structure and the change to kinetic energy in the non-radial direction (Suwa et al. 2019). Therefore, we should note that the same \dot{E}_{expl} in a multi-D model would have less ^{56}Ni than in a 1D model.

In fact, with the exception of particular model results (Bollig et al. 2021, discussed next), the multi-D self-consistent simulation has even more difficulty with ^{56}Ni synthesis than the estimate of this study (e.g., Bruen et al. 2022). Therefore, for the same synthesis conditions, the 1D model gives a robust maximum limit on the volume and the amount of ^{56}Ni synthesis. The additional ^{56}Ni amount newly occurring due to the multi-D effect will be discussed next.

3. [Additional mechanism to add ^{56}Ni]

Another possibility for an additional ^{56}Ni , and one of the most often cited candidates for a solution to this problem, is the ‘outflow’ from the PNS surface for several seconds of the post-explosion phase (e.g., Wongwathanarat et al. 2017; Witt et al. 2021). Recent detailed simulations have predicted proton-rich ejecta in the post-explosion ‘outflow’ (e.g., Bruenn et al. 2016). In particular, Bollig et al. (2021) have observed the downflow/outflow system that results in a smooth and efficient transition from the incoming flow to the outgoing flow, with the outflow providing ^{56}Ni to $\lesssim 0.05M_\odot$. However, we already found that the contribution of such replenishment is small for regular CCSNe explosions (Sawada & Suwa 2021). That is, this outflow system is part of an ‘energetic’ model of the state-of-the-art simulations that succeeds in producing sufficient amounts of ^{56}Ni , and it is debatable whether this outflow system contributes to canonical-CCSNe explosions.

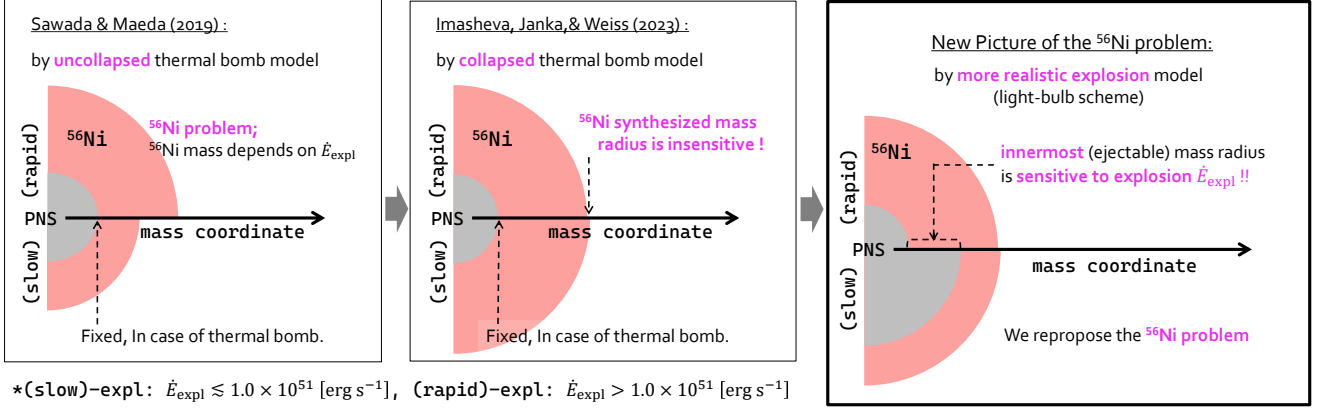


Figure 8. Schematic picture to the ‘ ^{56}Ni problem in CCSNe’ as suggested by the previous studies and this study, respectively. At first, [Sawada & Maeda \(2019\)](#) raised the ^{56}Ni problem because the ^{56}Ni synthesized region varies with the growth rate of the explosion energy \dot{E}_{expl} when an un-collapsed progenitor is used. When taking into account that the progenitor collapses just before the explosion, the ^{56}Ni synthesized region becomes insensitive to \dot{E}_{expl} , and thus, [Imasheva et al. \(2023\)](#) proposed a disappearance of the ^{56}Ni problem. However, this study re-proposes the ^{56}Ni problem on the grounds that while the ^{56}Ni synthesized region is insensitive to \dot{E}_{expl} , the ejectable innermost mass radius depends on the \dot{E}_{expl} , as calculated using the light-bulb scheme in which the PNS masses is determined self-consistently.

4. [Comparison to [Imasheva et al. \(2023\)](#)]

Finally, we compare our results with those of [Imasheva et al. \(2023\)](#) who just recently pointed out the most obvious doubts about the ‘ ^{56}Ni problems’. Figure 8 is a schematic comparison of our results with theirs. Their argument is that the correlation between \dot{E}_{expl} and ^{56}Ni disappears when the initial collapse is included, and that further initial collapse inversely results in more ^{56}Ni being synthesized in slower explosions. Noting that the innermost ejecta radius is fixed in the thermal bomb model, their argument is consistent with the present results where ^{56}Ni is synthesized to almost the same mass coordinate independent of \dot{E}_{expl} , shown in Figure 4. We also confirm that ^{56}Ni is synthesized slightly more outwardly in models with slower initial collapse (i.e., the $M_{\text{ZAMS}} = 19.5M_{\odot}$ model). The difference from their study is the treatment of the innermost mass coordinate of the ejecta, i.e., their inner boundary condition. Our explosion model determines the innermost mass coordinate of the ejecta self-consistently. We then found that the innermost material that could be ejected in the high- \dot{E}_{expl} model could not achieve the escape condition in the low- \dot{E}_{expl} model, leading to moving the innermost mass coordinate of the ejecta outward. In fact, for low \dot{E}_{expl} models, [Imasheva et al. \(2023\)](#) themselves had mentioned the possibility that some of the innermost material may be unable to achieve escape conditions, remain gravitation-

ally bound, and thus not contribute to the yield, and we confirmed this in this paper. Although our results are consistent with theirs, we confirm that ^{56}Ni problems reappear because the innermost ejecta radius shifts depending on the intensity of the \dot{E}_{expl} .

We conclude that the modern slow explosion ($\dot{E}_{\text{expl}} \lesssim 1 \text{ Bethe s}^{-1}$) can reproduce the observations of a standard Type II supernova. However, this is only a statement of a principal possibility. How much ^{56}Ni can be synthesized is an important benchmark for multidimensional self-consistent simulations, and it should be confirmed whether the median value for a standard Type II supernova ($\approx 0.03M_{\odot}$) is indeed achieved.

On the other hand, the ^{56}Ni problem clearly exists in the explosion mechanism of SE-SNe, that is, the modern slow explosions cannot reproduce the SE-SNe observations. As a simple and straightforward solution that satisfies the ^{56}Ni problem without fine-tuning, we conclude that the SE-SNe favors active explosions in the early stages of shock revival ($\dot{E}_{\text{expl}} \gtrsim 2 \text{ Bethe s}^{-1}$). Since such high explosion energies are probably inconsistent with the standard explosion mechanism, the ^{56}Ni problem may require a different explosion mechanism for the SE-SNe. [Anderson \(2019\)](#) had already suggested from observations, but our results once again imply significant differences in the progenitor structures and/or the explosion mechanism between type II and SE-SNe.

5. SUMMARY

In this paper, we investigated the effect of the explosion energy growth rate \dot{E}_{expl} on the behavior of ^{56}Ni nucleosynthesis in CCSNe. For numerical simulations, we employed the 1D Lagrangian hydrodynamic code in which neutrino heating and cooling terms are taken into account by the light-bulb approximation. The initial conditions are taken from Sukhbold et al. (2018), which have $M_{\text{ZAMS}} = 12.3, 16.0, 18.0,$ and $19.5M_{\odot}$.

Our first purpose was to present a detailed picture of ^{56}Ni nucleosynthesis in CCSNe with self-consistent explosion modeling. We found that ^{56}Ni is synthesized up to the almost same mass coordinate independent of \dot{E}_{expl} . We also found that in the low- \dot{E}_{expl} model, some of the innermost material that was ejected in the high- \dot{E}_{expl} model failed to achieve the escape condition, leading to moving the innermost mass coordinate of the ejecta to the outer positions. This means that while the ^{56}Ni nucleosynthesis volume is insensitive to the nature of the explosion, the ejected amount of ^{56}Ni is highly dependent on how much of the innermost PNS surface region is ejectable.

Furthermore, our other goal was to sort out the recent controversial ^{56}Ni problem. We found that there is a decreasing trend of the synthesized amount of ^{56}Ni toward decreasing \dot{E}_{expl} . Compared to observations, we found that the modern slow explosion ($\dot{E}_{\text{expl}} \lesssim 1$

Bethe s^{-1}) can reproduce the observations of a standard Type II supernova in a principal. However, this does not mean that the ^{56}Ni problem has been solved, and the ^{56}Ni synthesis ($M_{\text{Ni}} \approx 0.03M_{\odot}$) still remains an important benchmark for multi-D self-consistent simulations. It should be checked whether they are truly achieved. And extremely important are the comparison results with SE-SNe. We found that the median value of SE-SNe ($M_{\text{Ni}} \approx 0.07M_{\odot}$) is challenging to reproduce in the modern slow explosion ($\dot{E}_{\text{expl}} \lesssim 1$ Bethe s^{-1}). As a simple and straightforward solution that satisfies the amount of ^{56}Ni without fine-tuning, the SE-SNe favors active explosions in the early stages of shock revival ($\dot{E}_{\text{expl}} \gtrsim 2$ Bethe s^{-1}). Thus, we conclude that there are significant differences in the progenitor structures and/or the explosion mechanism between type II and SE-SNe.

Software: `blcode`, `torch`(Timmes 1999)

ACKNOWLEDGMENTS

The work has been supported by Japan Society for the Promotion of Science (JSPS) KAKENHI grants 21J00825, 21K13964 (RS), 18H05437, 20H00174, 20H01904, and 22H04571 (YS).

REFERENCES

- Anderson, J. P. 2019, A&A, 628, A7, doi: [10.1051/0004-6361/201935027](https://doi.org/10.1051/0004-6361/201935027)
- Arnett, W. D. 1982, ApJ, 253, 785, doi: [10.1086/159681](https://doi.org/10.1086/159681)
- Arnett, W. D., Bahcall, J. N., Kirshner, R. P., & Woosley, S. E. 1989, ARA&A, 27, 629, doi: [10.1146/annurev.aa.27.090189.003213](https://doi.org/10.1146/annurev.aa.27.090189.003213)
- Bethe, H. A., & Wilson, J. R. 1985, ApJ, 295, 14, doi: [10.1086/163343](https://doi.org/10.1086/163343)
- Bodansky, D., Clayton, D. D., & Fowler, W. A. 1968, ApJS, 16, 299, doi: [10.1086/190176](https://doi.org/10.1086/190176)
- Bollig, R., Yadav, N., Kresse, D., et al. 2021, ApJ, 915, 28, doi: [10.3847/1538-4357/abf82e](https://doi.org/10.3847/1538-4357/abf82e)
- Bruen, S. W., Sieverding, A., Lentz, E. J., et al. 2022, arXiv e-prints, arXiv:2211.12675, <https://arxiv.org/abs/2211.12675>
- Bruenn, S. W., Lentz, E. J., Hix, W. R., et al. 2016, ApJ, 818, 123, doi: [10.3847/0004-637X/818/2/123](https://doi.org/10.3847/0004-637X/818/2/123)
- Burrows, A., & Vartanyan, D. 2021, Nature, 589, 29, doi: [10.1038/s41586-020-03059-w](https://doi.org/10.1038/s41586-020-03059-w)
- Clifford, F. E., & Tayler, R. J. 1965, MmRAS, 69, 21
- Fowler, W. A., & Hoyle, F. 1964, ApJS, 9, 201, doi: [10.1086/190103](https://doi.org/10.1086/190103)
- Freiburghaus, C., Rembges, J. F., Rauscher, T., et al. 1999, ApJ, 516, 381, doi: [10.1086/307072](https://doi.org/10.1086/307072)
- Glas, R., Just, O., Janka, H. T., & Obergaulinger, M. 2019, ApJ, 873, 45, doi: [10.3847/1538-4357/ab0423](https://doi.org/10.3847/1538-4357/ab0423)
- Hamuy, M. 2003, ApJ, 582, 905, doi: [10.1086/344689](https://doi.org/10.1086/344689)
- Hix, W. R., & Thielemann, F.-K. 1999, ApJ, 511, 862, doi: [10.1086/306692](https://doi.org/10.1086/306692)
- Imasheva, L., Janka, H.-T., & Weiss, A. 2023, MNRAS, 518, 1818, doi: [10.1093/mnras/stac3239](https://doi.org/10.1093/mnras/stac3239)
- Iwamoto, K., Nomoto, K., Höflich, P., et al. 1994, ApJL, 437, L115, doi: [10.1086/187696](https://doi.org/10.1086/187696)
- Jerkstrand, A., Timmes, F. X., Magkotsios, G., et al. 2015, ApJ, 807, 110, doi: [10.1088/0004-637X/807/1/110](https://doi.org/10.1088/0004-637X/807/1/110)
- Jones, D. O., Foley, R. J., Narayan, G., et al. 2021, ApJ, 908, 143, doi: [10.3847/1538-4357/abd7f5](https://doi.org/10.3847/1538-4357/abd7f5)
- Lentz, E. J., Bruenn, S. W., Hix, W. R., et al. 2015, The Astrophysical Journal, 807, L31, doi: [10.1088/2041-8205/807/2/L31](https://doi.org/10.1088/2041-8205/807/2/L31)

Table 1. Summary of simulations

M_{ZAMS} [M_{\odot}]	$M_{s/k_b=4}$ ^a [M_{\odot}]	$\xi_{s/k_b=4}$ ^b	L_{ν_e} [10^{52}erg s^{-1}]	\dot{E}_{expl} ^c [10^{51}erg s^{-1}]	M_{PNS} ^d [M_{\odot}]	$M_{T_9=5}$ ^e [M_{\odot}]	$M_r(X_{56\text{Ni}} > 0.5)$ ^f [M_{\odot}]	$M_{56\text{Ni}}$ ^g [M_{\odot}]
12.3	1.462	0.837	1.4	0.46	1.464	1.514	1.523	0.049
			2	0.60	1.464	1.509	1.516	0.047
			3	1.04	1.458	1.507	1.512	0.049
			4	1.75	1.449	1.507	1.512	0.057
			5	2.88	1.427	1.510	1.514	0.078
16.0	1.618	0.700	2	0.48	1.617	1.655	1.659	0.039
			3	0.82	1.615	1.651	1.655	0.039
			4	1.35	1.605	1.650	1.653	0.045
			5	2.39	1.582	1.653	1.671	0.068
			6	3.47	1.561	1.651	1.656	0.087
			7	4.62	1.536	1.650	1.655	0.109
18.0	1.535	0.793	2	0.83	1.537	1.593	1.607	0.062
			3	1.06	1.537	1.593	1.600	0.059
			4	1.49	1.535	1.593	1.599	0.060
			5	2.12	1.530	1.593	1.600	0.065
			6	3.10	1.514	1.595	1.602	0.081
			7	4.23	1.514	1.608	1.615	0.112
19.5	1.714	0.762	2	0.70	1.912	1.962	1.970	0.054
			3	1.22	1.720	1.806	1.816	0.090
			4	1.64	1.717	1.801	1.811	0.089
			5	2.10	1.714	1.800	1.810	0.092
			6	2.80	1.709	1.801	1.810	0.097
			7	3.69	1.691	1.801	1.810	0.114

^a Mass Coordinate with $s = 4k_B$ baryon⁻¹.

^b Compactness parameter of $M_{s/k_b=4}$ which is defined as $(M_{s/k_b=4}/M_{\odot})/(R_{s/k_b=4}/1000\text{km})$.

^c Neutrino luminosity.

^d PNS mass which we define as the mass coordinate that experienced $r < 200$ km as the neutrino-driven wind and separate it from the ejecta.

^e Mass Coordinate of shock at a time when the post-shock temperature is $T = 5 \times 10^9$ K.

^f Outermost mass radius where the ^{56}Ni is $X_{56\text{Ni}} > 0.5$ synthesized.

^g ^{56}Ni mass computed in a post-process with the 640-isotope.

Li, W., Leaman, J., Chornock, R., et al. 2011, MNRAS, 412, 1441, doi: [10.1111/j.1365-2966.2011.18160.x](https://doi.org/10.1111/j.1365-2966.2011.18160.x)

Maeda, K., & Tominaga, N. 2009, Monthly Notices of the Royal Astronomical Society, 394, 1317, doi: [10.1111/j.1365-2966.2009.14460.x](https://doi.org/10.1111/j.1365-2966.2009.14460.x)

Magkotsios, G., Timmes, F. X., Hungerford, A. L., et al. 2010, ApJS, 191, 66, doi: [10.1088/0067-0049/191/1/66](https://doi.org/10.1088/0067-0049/191/1/66)

Magkotsios, G., Timmes, F. X., & Wiescher, M. 2011, ApJ, 741, 78, doi: [10.1088/0004-637X/741/2/78](https://doi.org/10.1088/0004-637X/741/2/78)

Marek, A., & Janka, H. T. 2009, ApJ, 694, 664, doi: [10.1088/0004-637X/694/1/664](https://doi.org/10.1088/0004-637X/694/1/664)

Martinez, L., Bersten, M. C., Anderson, J. P., et al. 2022, A&A, 660, A41, doi: [10.1051/0004-6361/202142076](https://doi.org/10.1051/0004-6361/202142076)

Mazzali, P. A., Deng, J., Maeda, K., et al. 2002, ApJL, 572, L61, doi: [10.1086/341504](https://doi.org/10.1086/341504)

Morozova, V., Piro, A. L., Renzo, M., et al. 2015, ApJ, 814, 63, doi: [10.1088/0004-637X/814/1/63](https://doi.org/10.1088/0004-637X/814/1/63)

Müller, B., Melson, T., Heger, A., & Janka, H.-T. 2017, MNRAS, 472, 491, doi: [10.1093/mnras/stx1962](https://doi.org/10.1093/mnras/stx1962)

Nomoto, K., Kobayashi, C., & Tominaga, N. 2013, ARA&A, 51, 457,

doi: [10.1146/annurev-astro-082812-140956](https://doi.org/10.1146/annurev-astro-082812-140956)

- O'Connor, E. P., & Couch, S. M. 2018, *ApJ*, 865, 81, doi: [10.3847/1538-4357/aadcf7](https://doi.org/10.3847/1538-4357/aadcf7)
- Ouchi, R., Maeda, K., Anderson, J. P., & Sawada, R. 2021, *ApJ*, 922, 141, doi: [10.3847/1538-4357/ac2306](https://doi.org/10.3847/1538-4357/ac2306)
- Rodríguez, Ó., Maoz, D., & Nakar, E. 2022, arXiv e-prints, arXiv:2209.05552. <https://arxiv.org/abs/2209.05552>
- Rodríguez, Ó., Meza, N., Pineda-García, J., & Ramirez, M. 2021, *MNRAS*, 505, 1742, doi: [10.1093/mnras/stab1335](https://doi.org/10.1093/mnras/stab1335)
- Saito, S., Tanaka, M., Sawada, R., & Moriya, T. J. 2022, *ApJ*, 931, 153, doi: [10.3847/1538-4357/ac6bec](https://doi.org/10.3847/1538-4357/ac6bec)
- Sawada, R., & Maeda, K. 2019, *ApJ*, 886, 47, doi: [10.3847/1538-4357/ab4da3](https://doi.org/10.3847/1538-4357/ab4da3)
- Sawada, R., & Suwa, Y. 2021, *ApJ*, 908, 6, doi: [10.3847/1538-4357/abd476](https://doi.org/10.3847/1538-4357/abd476)
- Seitenzahl, I. R., Timmes, F. X., Marin-Lafèche, A., et al. 2008, *ApJL*, 685, L129, doi: [10.1086/592501](https://doi.org/10.1086/592501)
- Smartt, S. J. 2009, *ARA&A*, 47, 63, doi: [10.1146/annurev-astro-082708-101737](https://doi.org/10.1146/annurev-astro-082708-101737)
- Sukhbold, T., Woosley, S. E., & Heger, A. 2018, *ApJ*, 860, 93, doi: [10.3847/1538-4357/aac2da](https://doi.org/10.3847/1538-4357/aac2da)
- Suwa, Y., & Tominaga, N. 2015, *Monthly Notices of the Royal Astronomical Society*, 451, 282, doi: [10.1093/mnras/stv901](https://doi.org/10.1093/mnras/stv901)
- Suwa, Y., Tominaga, N., & Maeda, K. 2019, *MNRAS*, 483, 3607, doi: [10.1093/mnras/sty3309](https://doi.org/10.1093/mnras/sty3309)
- Suwa, Y., Yamada, S., Takiwaki, T., & Kotake, K. 2016, *ApJ*, 816, 43, doi: [10.3847/0004-637X/816/1/43](https://doi.org/10.3847/0004-637X/816/1/43)
- Takiwaki, T., Kotake, K., & Suwa, Y. 2016, *Monthly Notices of the Royal Astronomical Society*, 461, L112, doi: [10.1093/mnrasl/slw105](https://doi.org/10.1093/mnrasl/slw105)
- Thielemann, F.-K., Nomoto, K., & Hashimoto, M.-A. 1996, *ApJ*, 460, 408, doi: [10.1086/176980](https://doi.org/10.1086/176980)
- Timmes, F. X. 1999, *ApJS*, 124, 241, doi: [10.1086/313257](https://doi.org/10.1086/313257)
- Timmes, F. X., & Swesty, F. D. 2000, *ApJS*, 126, 501, doi: [10.1086/313304](https://doi.org/10.1086/313304)
- Von Neumann, J., & Richtmyer, R. D. 1950, *Journal of Applied Physics*, 21, 232, doi: [10.1063/1.1699639](https://doi.org/10.1063/1.1699639)
- Witt, M., Psaltis, A., Yasin, H., et al. 2021, *ApJ*, 921, 19, doi: [10.3847/1538-4357/ac1a6d](https://doi.org/10.3847/1538-4357/ac1a6d)
- Wongwathanarat, A., Janka, H.-T., Müller, E., Pllumbi, E., & Wanajo, S. 2017, *ApJ*, 842, 13, doi: [10.3847/1538-4357/aa72de](https://doi.org/10.3847/1538-4357/aa72de)
- Woosley, S. E., Arnett, W. D., & Clayton, D. D. 1973, *ApJS*, 26, 231, doi: [10.1086/190282](https://doi.org/10.1086/190282)
- Woosley, S. E., Heger, A., & Weaver, T. A. 2002, *Reviews of Modern Physics*, 74, 1015, doi: [10.1103/RevModPhys.74.1015](https://doi.org/10.1103/RevModPhys.74.1015)
- Woosley, S. E., & Weaver, T. A. 1995, *ApJS*, 101, 181, doi: [10.1086/192237](https://doi.org/10.1086/192237)

APPENDIX

A. ^{56}Ni SYNTHESIS CONDITION

Here, we briefly review the general features of ^{56}Ni nucleosynthesis in CCSNe, which is classically well enough understood (e.g., [Bodansky et al. 1968](#); [Woosley et al. 1973](#); [Hix & Thielemann 1999](#)). To illustrate the condition of ^{56}Ni synthesis, for simplicity, we use parameterized adiabatic expansion profiles. Let us focus on a certain Lagrangian particle. Assuming that a passing shock wave heats and compresses the particle to peak temperature T_0 and peak density ρ_0 , and then it expands and cools in a constant T^3/ρ track, we can write the temperature and density evolution ([Woosley et al. 1973](#)) as

$$\begin{aligned} T(t) &= T_0 \exp(-t/3\tau_{\text{dyn.}}), \\ \rho(t) &= \rho_0 \exp(-t/\tau_{\text{dyn.}}), \end{aligned} \quad (\text{A1})$$

where the expansion timescale of the ejecta τ is the following ([Fowler & Hoyle 1964](#));

$$\tau_{\text{dyn.}} = (24\pi G \rho_0)^{-1/2} \approx 446/\rho_0^{1/2} \text{ sec.} \quad (\text{A2})$$

This expansion trajectory reproduces the general temperature and density trajectories in spherically symmetric or multi-dimensional CCSNe explosions, especially in the explosive nucleosynthesis region (e.g., [Magkotsios et al. 2010, 2011](#); [Jerkstrand et al. 2015](#)). We calculate a reaction network of 640 nuclear species with `torch` code ([Timmes 1999](#)), with the initial composition $X(^{28}\text{Si}) = 1$. We then check the behavior of ^{56}Ni nucleosynthesis using expansion profiles with peak temperature T_0 and peak density ρ_0 as parameters.

Figure 9 shows the abundance of synthesized ^{56}Ni as a function of the peak temperature T_0 in the adiabatic expansion profile. When the peak temperature is $T_9 \gtrsim 5$ ($T_9 \equiv T/10^9$ K), we can see that a sizable amount of ^{56}Ni is synthesized, almost independent of the peak density ρ_0 . In this temperature region, ^{28}Si is wholly depleted at the same time as satisfying ^{56}Ni synthesis, so this explosive nucleosynthesis is referred to as ‘complete Si burning’. This depletion of ^{28}Si occurs when the lifetime over which ^{28}Si burns up is much shorter than the given expansion time scale, i.e., $\tau(^{28}\text{Si}) \ll \tau_{\text{dyn.}}$. According to [Woosley et al. \(1973\)](#), to estimate this condition quantitatively, we define the depletion point of ^{28}Si as when its mass fraction falls below about 0.005 (i.e., $X_f(^{28}\text{Si}) < 0.005$). Then, complete Si combustion is estimated to occur under the following initial conditions;

$$T_9 \gtrsim 5.0 \times \left(\frac{\rho_0}{10^6 \text{ g cm}^{-3}} \right)^{1/68} \quad (\text{A3})$$

This implies that an initial temperature must exceed $T_9 \approx 5$ to promote the depletion of ^{28}Si in order for the complete silicon burning to occur at a reasonable density. This estimate is roughly consistent with our numerical result in Figure 9.

In complete Si burning, the forward and reverse reactions in the main reaction channel proceed much faster than the time scale of the change in thermal conditions. The compositions thus basically follow the Nuclear Statistical Equilibrium (NSE), except for the slow triple-alpha process. Then, as the temperature decreases rapidly, the reaction rates decrease and the abundance pattern ‘freezes-out’ ([Hix & Thielemann 1999](#)). In NSE, the composition ratio is determined to minimize the Helmholtz free energy ($\mathcal{F} = (U - \mathcal{Q}) - TS$) for the nuclide mass fraction ([Clifford & Tayler 1965](#)). When the temperature is not too high ($T_9 < 10$), the binding energy per nucleon (BEN) $\mathcal{Q} = B/A$ roughly determines the abundance pattern of NSE. In environments where the number of protons and neutrons is almost equal ($Y_e \approx 0.5$), the most abundant isotope in NSE is ^{56}Ni . Therefore, the main synthesis process of ^{56}Ni in the SNe explosion is not a two-/three-body reaction, but a ‘freezes-out’ of the NSE abundance pattern that occurred via the ‘photodisintegration-rearrangement reactions’ associated with the photodisintegration of ^{28}Si .

Next, Figure 10 shows what the ^{56}Ni synthesis would be in a different environment for Y_e with different peak temperatures. We can clearly see that while ^{56}Ni synthesis in the proton-rich environment ($Y_e > 0.5$) is relatively the same as that in the $Y_e \approx 0.5$ environment, its synthesis is quite suppressed in the neutron-rich environment ($Y_e < 0.5$). As explained by [Seitenzahl et al. \(2008\)](#), Y_e dependence of nickel nucleosynthesis can be understood qualitatively by focusing on the BEN, $\mathcal{Q} = B/A$, and the Helmholtz free energy \mathcal{F} .

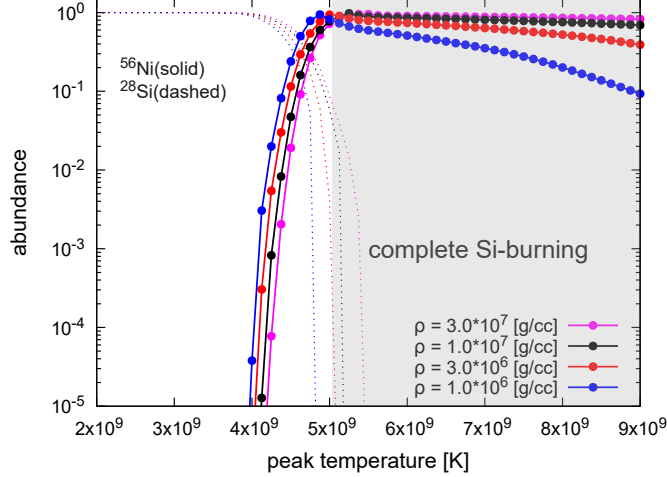


Figure 9. The abundance of synthesized ^{56}Ni as a function of peak temperature T_0 with the peak density ρ_0 at $Y_e = 0.5$, calculated using the adiabatic expansion profile of Eq. (A1).

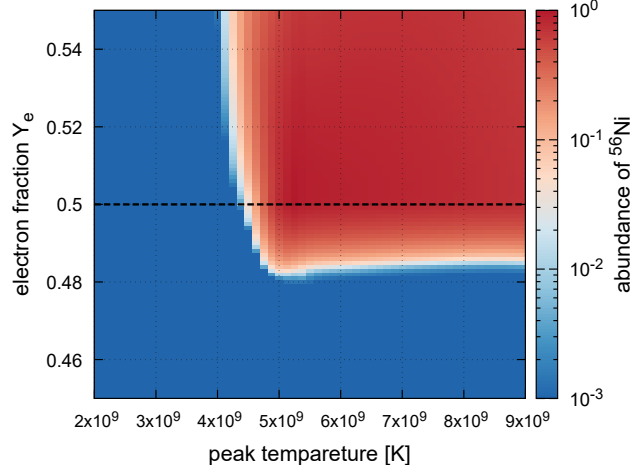


Figure 10. The abundance of synthesized ^{56}Ni in the peak temperature T_0 and the initial electron fraction Y_e plane at the peak density $\rho_0 = 10^7 \text{ g cm}^{-3}$, calculated using the adiabatic expansion profile of Eq. (A1).

Figure 11 (left) illustrates the BEN of various Ni-isotopes with blue crosses, where the number of protons per nucleon ($Y_p = Z/A$, which corresponds to Y_e) on the horizontal axis. To analyze stability, we consider a mixed composition of ^{56}Ni plus an appropriate number of free protons or free neutrons (^{56}Ni + nucleons) to match any Y_e . The mean BEN of the mixed composition is calculated as $\bar{Q} = \sum_i Q_i n_i / n_B$, where Q_i is the binding energy of the nucleus i and $Q_{\text{neut}} = Q_{\text{prot}} = 0$. By comparing the BENs for each Y_e , we find that the single Ni-isotope is significantly more stable than the ^{56}Ni + nucleons mixture in the neutron-rich region ($Y_e < 0.5$), but not in the proton-rich region ($Y_e \geq 0.5$). While this picture is somewhat modified when entropy is taken into account, this simple discussion shows that ^{56}Ni synthesis is suppressed in the neutron-rich region.

Figure 11 (right) shows Helmholtz free energies ($\mathcal{F} = (U - Q) - TS$) for a single composition of only Ni isotopes and, as before, for a mixed composition of ^{56}Ni plus an appropriate number of free protons or free neutrons. Helmholtz free energy was calculated using Helmholtz EoS (Timmes & Swesty 2000) with $T = 5 \times 10^9 \text{ K}$ and $\rho = 10^7 \text{ g cm}^{-3}$ fixed. In an environment with the same T and ρ , the internal energy can be considered to be almost constant, $U \approx \text{Const}$. The BEN term, Q , then contributes to the Helmholtz free energy on the order of $1 \text{ MeV/nuclear} \approx \mathcal{O}(10^{18}) \text{ erg g}^{-1}$. For the TS term, the entropy is increased by the free nucleons in the ^{56}Ni + nucleon mixture composition compared to the single Ni-isotope composition. It thus works toward lowering the Helmholtz free energy on the order of $\mathcal{O}(10^{17}) \text{ erg}$

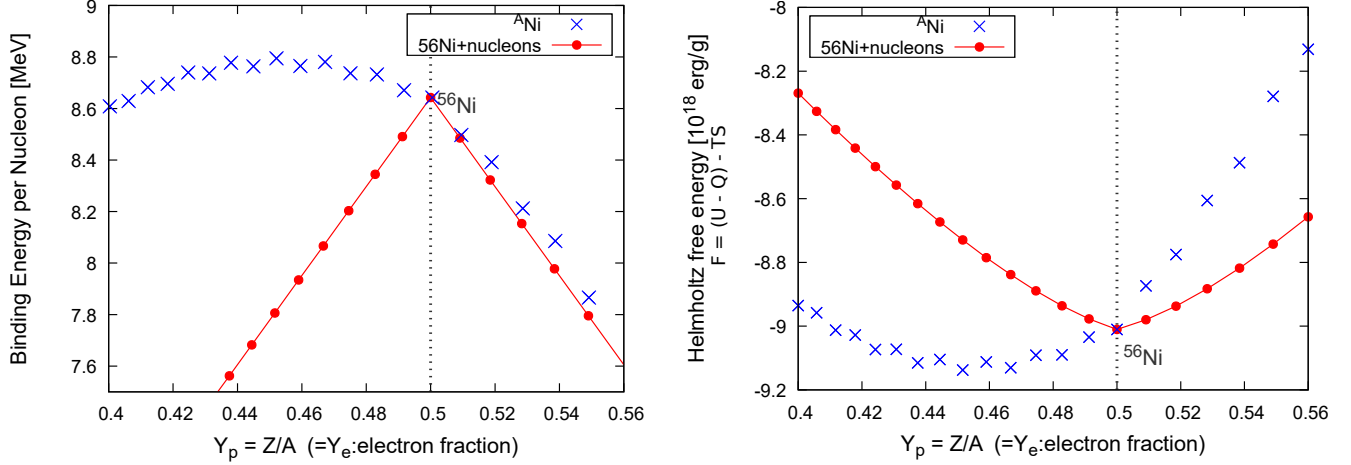


Figure 11. Binding energy per nucleon (left) and the Helmholtz free energy per nucleon (right) with the number of protons per nucleon $Y_p = Z/A$ (corresponds to Y_e , and $28/Y_e$ corresponds to the mass number A of each Ni isotope) on the horizontal axis. The blue crosses show the binding energy per nucleon (BEN) of the Ni-isotope, and the red circles indicate the mean BEN of a mixed composition, which is mixed with ^{56}Ni and an appropriate number of free protons or free neutrons for any given Y_e (^{56}Ni + nucleons). The mean BEN of the mixed composition is derived by $\bar{Q} = \sum_i Q_i n_i / n_B$. The Helmholtz free energies were calculated using Helmholtz EoS (Timmes & Swesty 2000) with $T = 5 \times 10^9$ K and $\rho = 10^7$ g cm $^{-3}$ fixed.

g^{-1} . Therefore, in the proton-rich region ($Y_e \geq 0.5$), the difference in BEN between the ^{56}Ni + nucleon mixture and the single Ni-isotope is $\Delta Q \lesssim \mathcal{O}(10^{17})$ erg g^{-1} , which is not much larger than the correction by entropy enhancement. As a result, the correction for the entropy enhancement due to the free nucleon makes the ^{56}Ni + nucleon mixture more stable. On the other hand, in the neutron-rich region ($Y_e < 0.5$), the difference in BEN is $\Delta Q \sim \mathcal{O}(10^{18})$ erg g^{-1} , which is sufficiently larger than the effect of the correction by entropy enhancement, and thus the single Ni-isotope composition is more stable, as predicted from the BEN behavior.

To summarize the above discussion, in the temperatures region where $T_9 \gtrsim 5$ are attained behind the shock, NSE is achieved except for the slow triple-alpha process. Thus, the abundance pattern depends only on Y_e and the entropy, and is dominated by iron-group elements (e.g., Hix & Thielemann 1999). The most abundant element in this region of complete Si burning with alpha-rich freeze-out is ^{56}Ni , provided $Y_e \gtrsim 0.5$. The ^{56}Ni synthesis conditions in CCSNe explosion are an environment where the peak temperature $T_9 \gtrsim 5$ is experienced by the shock and the electron fraction of the material is $Y_e \gtrsim 0.5$.